

ARTICLE OPEN

‘Eastern African Paradox’ rainfall decline due to shorter not less intense Long Rains

Caroline M. Wainwright^{1,2}, John H. Marsham^{3,4}, Richard J. Keane^{3,5}, David P. Rowell⁵, Declan L. Finney³, Emily Black^{1,2} and Richard P. Allan^{1,6}

An observed decline in the Eastern African Long Rains from the 1980s to late 2000s appears contrary to the projected increase under future climate change. This “Eastern African climate paradox” confounds use of climate projections for adaptation planning across Eastern Africa. Here we show the decline corresponds to a later onset and earlier cessation of the long rains, with a similar seasonal maximum in area-averaged daily rainfall. Previous studies have explored the role of remote teleconnections, but those mechanisms do not sufficiently explain the decline or the newly identified change in seasonality. Using a large ensemble of observations, reanalyses and atmospheric simulations, we propose a regional mechanism that explains both the observed decline and the recent partial recovery. A decrease in surface pressure over Arabia and warmer north Arabian Sea is associated with enhanced southerlies and an earlier cessation of the long rains. This is supported by a similar signal in surface pressure in many atmosphere-only models giving lower May rainfall and an earlier cessation. Anomalously warm seas south of Eastern Africa delay the northward movement of the tropical rain-band, giving a later onset. These results are key in understanding the paradox. It is now a priority to establish the balance of mechanisms that have led to these trends, which are partially captured in atmosphere-only simulations.

npj Climate and Atmospheric Science (2019)2:34; <https://doi.org/10.1038/s41612-019-0091-7>

INTRODUCTION

The March, April and May (MAM) ‘Long Rains’ of Eastern Africa have historically been the major rainfall and primary agricultural season for much of the region^{1,2}. Since around 1985 the rains have declined, with major consequences for livelihoods^{1–6}. In contrast, climate model projections show increased long-rains rainfall: this has been termed the ‘Eastern African climate change paradox’ that has been used to question the reliability of the projections^{5,7} and so arguably restricts their utility for informing suitable adaptation measures⁶.

Shortage of in situ observations makes assessment of regional rainfall trends across Africa challenging, yet the recent drying of the Eastern African long rains appears robust across datasets^{4,6,8}, with a drying in March, April, and May⁶. Coupled Model Intercomparison Project Phase 5 (CMIP5) simulations fail to consistently capture the MAM Eastern African drying with around half simulating a drying, and half a wetting⁶, while most atmosphere-only (AMIP) simulations, driven by observed sea surface temperature (SST) and realistic radiative forcings, correctly capture the drying^{3,6}. The observed drying is thus partly explained by SSTs^{2,3,9}. Comparison of the observed long rains trend with a range of trends from control runs of CMIP5 coupled models, in which anthropogenic forcing (and external natural forcing) are absent, indicates that the observed rainfall trend is unlikely to be entirely consistent with natural variability⁶. Mechanisms have been proposed linking the decline in the long rains with decadal variability in the Pacific Ocean^{1–5}. Specifically, changes in the zonal SST gradient in the Pacific¹⁰, warming of the Indo-Western Pacific

SSTs (with anomalous warm water transported from the tropical western Pacific to the Indian Ocean by Indonesian throughflow¹¹) and enhanced convection over the Western Equatorial Pacific, are associated with an anomalous Walker circulation over the Indian Ocean. Strengthening of the upper level easterlies and the descending branch lead to increased subsidence over Eastern Africa and reduced precipitation^{2,5,7}. However, there is limited evidence for the Indian Ocean Walker Cell extending over the Horn of Africa¹, and an equatorial zonal circulation cell is not present in boreal spring¹², although modulation of subsidence over Eastern Africa by upper level easterlies over the Indian Ocean has also been proposed¹.

Projections of changes in the onset and cessation of wet seasons across Africa under future climate change, produced using CMIP5 models, show the onset and cessation of the Eastern African October–December “short rains” getting later, while the cessation of the long rains is projected to get earlier¹³. Changes in the timing of onset and cessation across interior Africa (0–35°E) have been linked to changes in the progression of the tropical rain-band and the Saharan Heat Low (SHL)¹³. A stronger SHL (amplified by a water vapour—greenhouse gas warming feedback^{14,15}), leads to a northward shift in the tropical rain-band during the boreal summer and a delayed retreat of the rain-band southwards¹³. This delayed retreat may be associated with the later onset and cessation of the short rains.

Here, specific characteristics of the long rains decline are investigated, and a regional mechanism is proposed that explains both the observed decline, and the partial recovery since the late 2000s.

¹Department of Meteorology, University of Reading, Reading, UK; ²National Centre for Atmospheric Science (NCAS), Reading, UK; ³School of Earth and Environment, University of Leeds, Leeds, UK; ⁴National Centre for Atmospheric Science (NCAS), Leeds, UK; ⁵Met Office, Exeter, UK and ⁶National Centre for Earth Observation, University of Reading, Reading, UK
Correspondence: Caroline M. Wainwright (c.wainwright@reading.ac.uk)

Received: 2 May 2019 Accepted: 15 August 2019

Published online: 12 September 2019

RESULTS

Figure 1a shows the decline in Eastern Africa MAM rainfall during 1998–2008 relative to 1986–1997, and recent recovery from 2010 onwards, although with high year to year variability. The time-series is divided into three periods: a wetter period (1986–1997, P1), a drier period (1998–2008, P2) and the recent partial recovery (2009–2018, P3). Analysis of the seasonal cycle (Fig. 1b) reveals that the decrease in rainfall during P2 is clearly associated with a delayed onset (Fig. 1c, 4.9 days on average) and earlier cessation (Fig. 1d, 2.2 days on average), rather than a change in seasonal maximum daily rainfall as often assumed. Onset in P3 recovers to P1 values (Fig. 1e), while cessation in P3 partially recovers but is

still earlier than during P1 (Fig. 1f). Supplementary Fig. 2 shows the onset and cessation dates for individual years. These observed changes in seasonality are not fully explained by the warming of the Indo-Western Pacific SSTs altering subsidence over Eastern Africa since there is no decrease in seasonal maximum in area-averaged daily rainfall during P2 (Fig. 1b).

A delayed and then faster movement of the tropical rain-band northwards across Eastern Africa during the boreal spring could explain later onset and earlier cessation (Supplementary Fig. 3). Previous studies, using multiple observational datasets, found wetting at the northern and southern limits of the tropical rain belt extent during June–August and December–February over

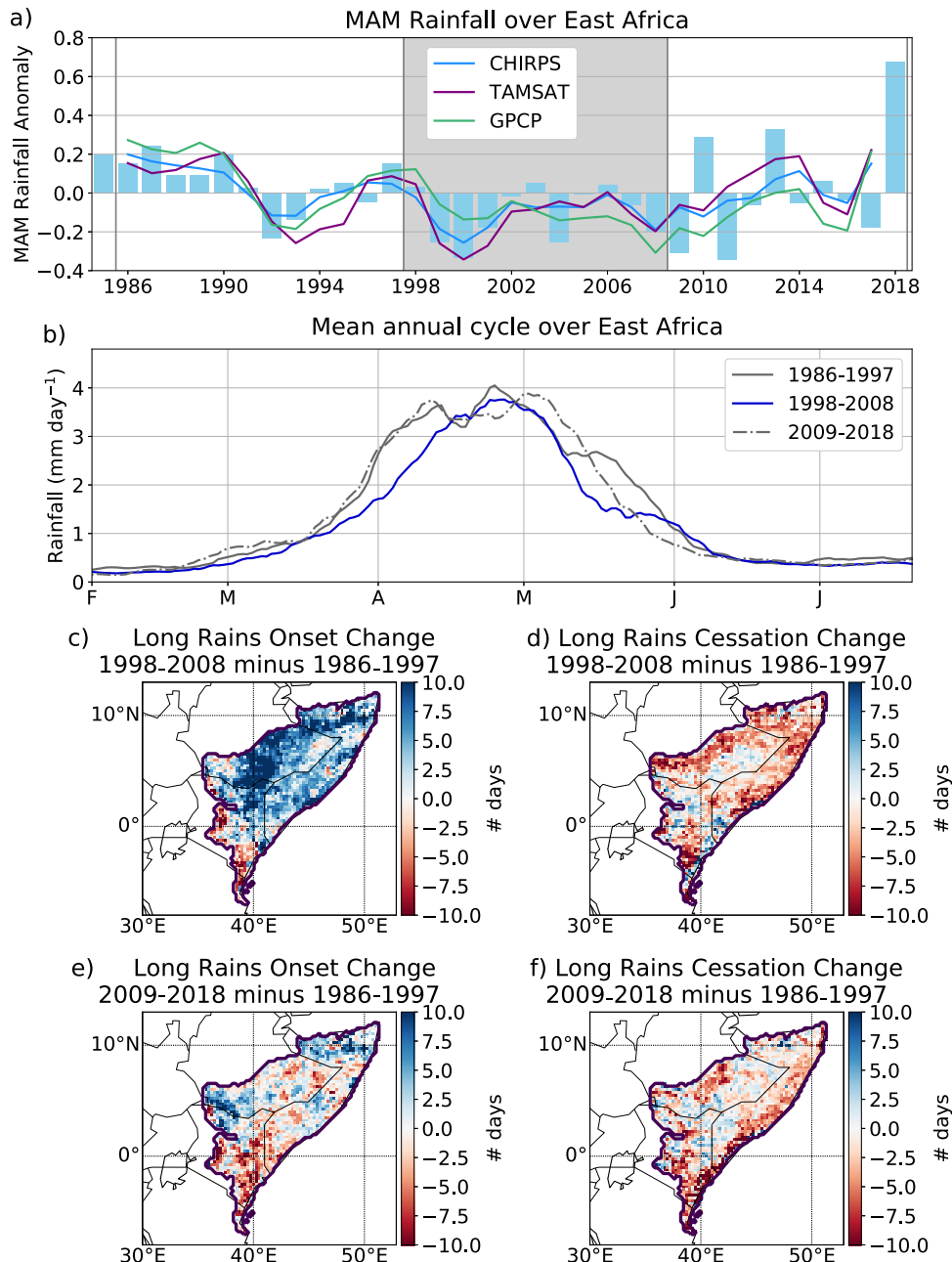


Fig. 1 Changes in seasonality of the long rains. **a** MAM rainfall anomaly over Eastern Africa (see region in **c–f**) 1985–2018 from CHIRPS, TAMSAT and GPCP. The bars represent the anomaly for each year (CHIRPS); the lines are smoothed using a 3 year moving average. **b** Mean seasonal cycle over Eastern Africa from CHIRPS over the 3 periods of study. **c, d** Maps showing the mean change in onset (**c**) and cessation (**d**) date of the long rains from 1986–1997 to 1998–2008. Onset and cessation dates were calculated using CHIRPS data and the method of Dunning et al.⁴³ (see methods). The purple contour demarcates the region used for Eastern Africa. **e, f** As (**c, d**), but comparing 2009–2018 with 1986–1997

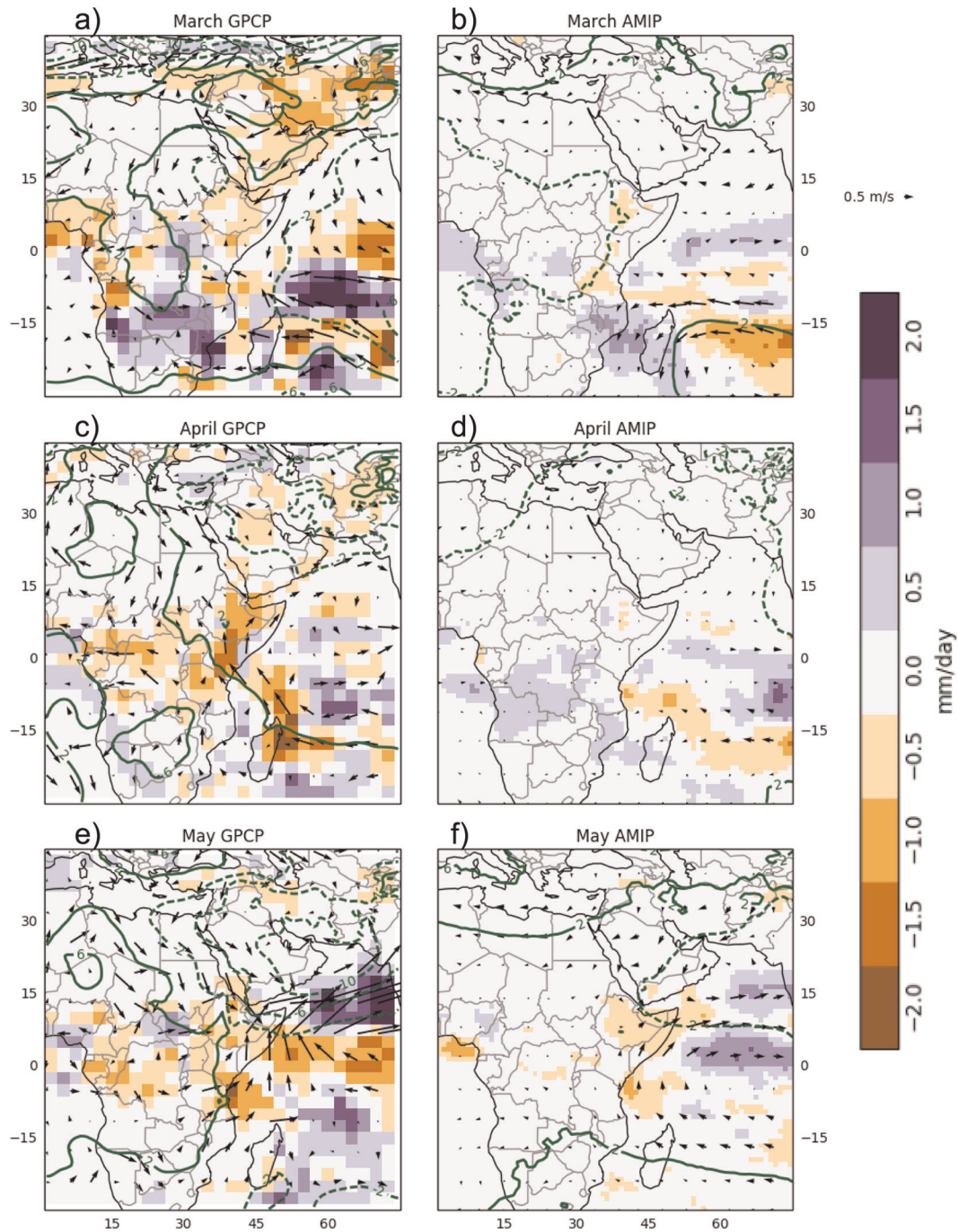


Fig. 2 Change in precipitation, geopotential height and 850 hPa winds for P2 minus P1. Change in precipitation (coloured shading), 850hPa geopotential height (m, green contours: solid lines represent positive values and dashed lines represent negative values) and 850 hPa winds (black arrows), for the period P2 minus period P1, for March (**a, b**), April (**c, d**) and May (**e, f**). Data for (**a, c, e**) are from ERA-Interim (wind and geopotential height) and GPCP (rainfall) and for (**b, d, f**) are from the AMIP multi-model mean (all variables)

1983–2008, with central Africa drying during MAM over the same period^{8,9}, consistent with a faster progression of the rain-band.

A recent study highlighted that under future climate change the strengthened SHL delays the southward progression of the rain-band across Africa, giving a later cessation and onset¹³. The recent observed faster northward movement of the rain-band in MAM therefore similarly suggests the SHL or a comparable mechanism may play a role in the earlier long-rains cessation revealed in Fig. 1. Following this study¹³, here changes in a different, proximal, heat low are investigated, to ascertain whether this influences the recent changes in the timing of the long rains over Eastern Africa.

Early cessation

Focusing on the early cessation, the Arabian Heat Low is a dominant feature over the Arabian Peninsula in spring and summer¹⁶, which interacts with the Somali Jet and Indian Monsoon^{17–19}. Figure 2 (and Supplementary Fig. 6) reveals a strong decrease in geopotential height over Arabia and the adjacent Arabian Sea in May in ERA-Interim from P1 to P2 (−8.46 m over 50–75°E, 10–25°N). This is also present in April (further north), is seen in other reanalyses (NCEP and MERRA) and is robust to changing periods of the composite (for P3–P1 see Supplementary Fig. 5 and Supplementary Fig. 6). The decrease in

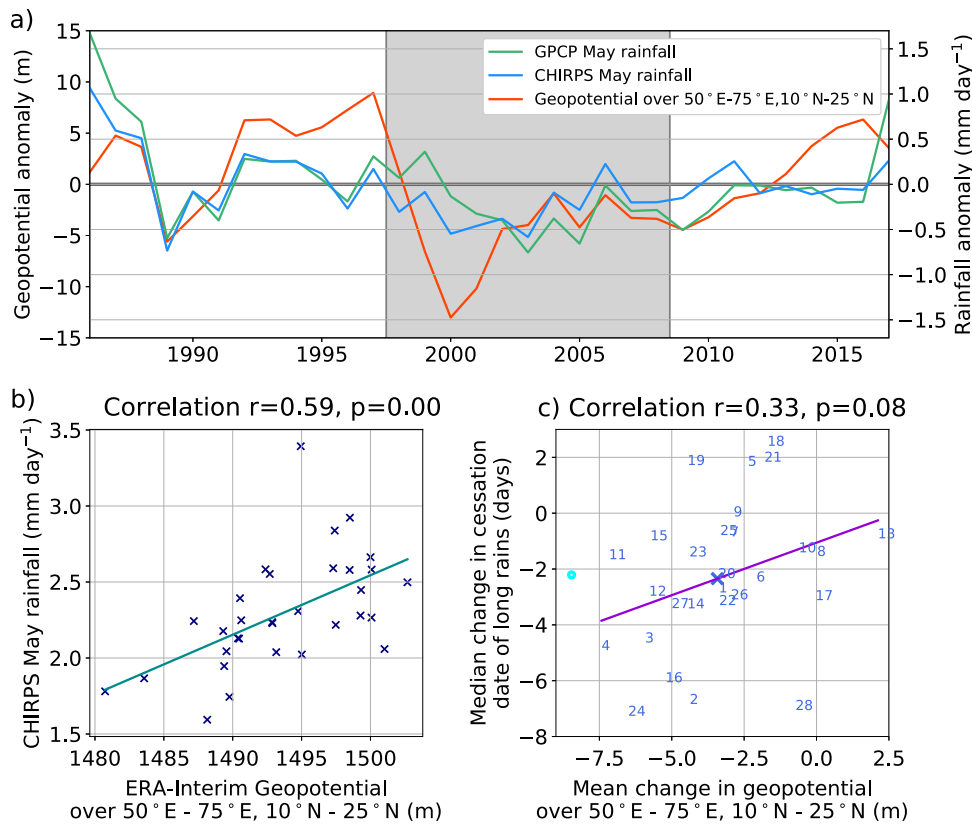


Fig. 3 Relationship between changes in geopotential over the north Arabian Sea and changes in East African May rainfall. **a, b** Mean May 850 hPa geopotential height over the North Arabian Sea from ERA-Interim and mean May precipitation over East Africa from GPCP and CHIRPS over 1986–2018 smoothed with a 3 year moving average. The corresponding scatter plot (CHIRPS) is shown in **(b)**. Correlation was calculated on the unsmoothed time-series. **c** The median change in cessation date of the long rains over East Africa from P1 to P2 in each AMIP model is plotted against the mean change in 850 hPa geopotential height over the north Arabian Sea from P1 to P2. The numbers correspond to the numbers for each AMIP model in Table 1 (methods); the cross shows the multi-model mean. The circle shows the change in geopotential height was calculated from ERA-Interim, and the change in cessation from the cessation dates computed using CHIRPS data

geopotential height is expected to draw the rain-band northwards faster and further, consistent with the observed and analysed rainfall changes (Figs. 1, 2, Supplementary Fig. 4). ERA-Interim captures the drying in Central and Eastern Africa in May, and the northward shift in Indian Ocean and Western India rainfall seen in observations²⁰ (Supplementary Fig. 4). The long rains correspond to the seasonal northerly-to-southerly reversal of the Somali Jet off the Horn of Africa, as the tropical rain-band crosses Eastern Africa. During P2 the southerlies are enhanced across Eastern Africa in May (Fig. 2), consistent with the earlier cessation of the faster propagating rain-band. Temperatures over the Arabian Peninsula increased over 1979–2009²¹, consistent with a pressure and geopotential height decrease. Furthermore, Arabian July–September temperatures exhibited a somewhat step-wise increase in the mid-1990s²², coincident with the Eastern African rainfall decline.

The decline in Eastern African May rainfall from 1998/9 onwards (coincident with the decrease in MAM rainfall) followed the decrease in geopotential height over Arabia starting in 1997 (Fig. 3). The correlation between the geopotential height and May rainfall (Climate Hazards Group infra-red Precipitation with Stations (CHIRPS)) time-series is moderate ($r = 0.59$), but significant at the 1% significance level (Fig. 3a, b). This correlation increases with smoothing, which suggests that both are driven, at least to some extent, by a common relatively persistent driver, with SSTs the most obvious candidate. This relationship might also address some of the low predictability of MAM rainfall on a seasonal time-scale^{23,24}.

The AMIP multi-model mean captures the drying across Eastern Africa in March and May and the increase in the strength of the Somali Jet in May (Fig. 2). It also captures the decrease in geopotential height in May over the north Arabian Sea (Fig. 2f), although the decrease is further southeast than in ERA-Interim, and restricted to over the ocean, not extending sufficiently over Arabia (Fig. 2 and Supplementary Fig. 6). The decrease in precipitation and geopotential height are of lower magnitude than the observed changes which may be linked to the lack of drying across the CMIP5 simulations. The assimilation of observations into ERA-Interim helps capture the trends compared with AMIP. AMIP simulations struggle to fully capture the response over land to SST and other forcings^{25,26}. Summertime dust increases over Arabia from 1997 to 2009 have been shown to deepen the Arabian Low in simulations²⁶, suggesting that the dust trend may influence Eastern African MAM rainfall.

We correlate the change in May geopotential height southeast of Arabia (where the AMIP models give the largest pressure decrease and ERA-Interim also shows a decrease) with both the change in May rainfall and the change in long rains cessation over Eastern Africa across the AMIP simulations (Fig. 3 and Supplementary Fig. 7). The correlation ($r = 0.33$) shows that the spread in the geopotential height decrease between models explains some of their range in the change in May rainfall and cessation date of the long rains. The multi-model mean captures the interannual correlation between the geopotential height over Arabia and the northern Arabian Sea and Eastern African May rainfall (Supplementary Fig. 8), with 25 out of 28 models capturing the positive

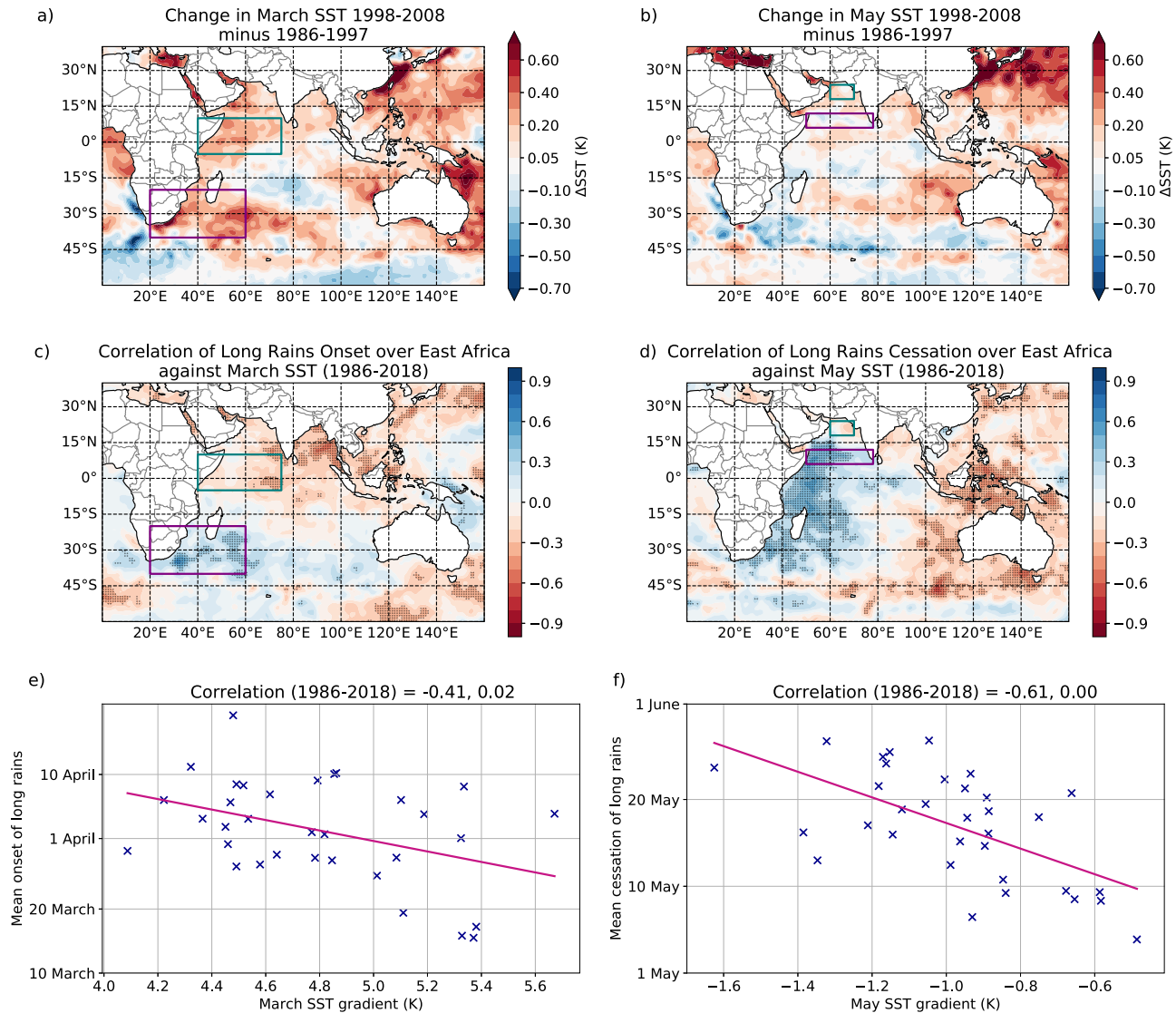


Fig. 4 Changes in March/May SST and relationship with Long Rains onset/cessation. **a, b** Change in March (**a**) and May (**b**) SST from P1 to P2 from HadISST. **c, d** Correlation (Pearson correlation coefficient) of onset (**c**) and cessation (**d**) date for the long rains across East Africa with March (**c**) and May (**d**) SST over 1986–2018. Onset and cessation dates were calculated using CHIRPS data and the method of Dunning et al.⁴³ (see methods). Stippling indicates a p value less than 0.1. **e, f** Scatter plot of the SST gradient in March/May (green box minus purple box) with the mean onset/cessation date from CHIRPS across East Africa for each year. The values quoted in the title are the r and p values calculated using Pearson correlation coefficient

correlation and 11 out of 28 models exhibiting a statistically significant interannual correlation. The AMIP simulated geopotential height changes are therefore important for explaining inter-model variations in the change in long-rains cessation, May rainfall change and the total MAM rainfall.

From P1 to P2, May SST increased more over the very north Arabian Sea than further south in the Indian Ocean (Fig. 4b). Warm May SSTs in the Indian Ocean are associated with a later cessation (Fig. 4d), but this correlation is reversed over the very north Arabian Sea (north of 15–20°N). We suggest that these changes in SST gradient across the Arabian Sea are associated with both the rainfall variability and its trend, with warmer SSTs to the north and cooler SSTs to the south initiating a pressure gradient across the Arabian Sea, drawing the rain-band north. Also, warmer SSTs to the north will favour moist convection there. The withdrawal of rainfall from Eastern Africa at the end of the long rains has previously been associated with the establishment of a low-pressure zone and active convection in the Arabian Sea²⁷. Two regions²⁸ were chosen to calculate the north–south SST gradient

across the Arabian Sea (Fig. 4f), which correlates with the long-rains cessation at -0.61 . The correlation was tested for robustness using 10 SST realisations (see methods) and all correlations were found to be significant, with a range of -0.45 to -0.70 across the 10 realisations. This supports the hypothesis that the rain-band has been drawn north by the warmer SSTs and the associated low-pressure, with an earlier cessation linked with relatively warmer SSTs to the north from P1 to P2. Comparing P3 with P2 (Supplementary Fig. 9), the SST has warmed more over the very north Arabian Sea, but contrast in warming is less, contributing to the partial recovery in long rains cessation, amongst other factors.

Late onset

Turning to the late onset, warming SSTs south of Madagascar (Fig. 4a) are associated with reduced March rainfall and later onsets (Fig. 4c), as warmer SSTs to the south delay the northward progression of the rain-band. Figure 4e shows a correlation of -0.41 (-0.29 to -0.48 across 10 realisations of HadISST) between

long rains onset and the southern-hemisphere SST gradient. From P2 to P3 March SST cooled south of Madagascar (Supplementary Fig. 9), potentially explaining the recent recovery in onset. Furthermore, during P2 the northerlies are enhanced in March (Fig. 2), also consistent with the delayed onset.

Future climate change

Sub-tropical land is expected to warm faster than tropical oceans under climate change²⁹, which together with water–vapour feedbacks can deepen sub-tropical heat lows, affecting rain-band progression^{13–15,30,31}. CMIP5 projections for 2080–2100 suggest a greater and more extensive deepening of the SHL compared to the Angola Low¹³. This leads to a strengthening north–south asymmetry with the rain-band moving further north in boreal summer, but not further south in austral summer. CMIP5 projections also show earlier onset and earlier cessation for Eastern Africa in MAM¹³. Considering the regional mechanisms identified here, projections under RCP 8.5 show a greater increase in geopotential height over the Indian Ocean compared with Arabia in May and strengthening of the Somali Jet (Supplementary Fig. 10), consistent with projections of an earlier cessation of the long rains¹³. In March, the surface temperature increases more in the western Indian Ocean than south of Madagascar, which combined with the southerly wind anomaly is consistent with projections of earlier onset¹³. Thus, CMIP5 projections of earlier onset and cessation are consistent with the mechanism we have identified to describe the recent decline. The overall increase in long-rains rainfall projected under future climate change³² (that is less than the projected increase in the short rains)⁶, is therefore the consequence of little change in overall season length¹³ and an increase in the intensity of rainfall on individual days^{13,32,33}.

DISCUSSION

In summary, we find that the observed decline in Eastern African Long Rains is characterised by a shortening of the rainy season (with later onset and earlier cessation) rather than by a decrease in the peak daily rainfall. The cause of the shortening is a faster movement of the rain-band over Eastern Africa during the boreal spring. This is a consequence of warmer SSTs to the north during boreal summer and to the south during austral summer, which leads to an increased pressure gradient and hence to more rapid travel of the rain-band during the whole January–August period. The hypothesis that reduced pressure over Arabia and the adjacent ocean influences rain-band progression is supported by the fact that this pressure change explains some of the variation in May rain change across the AMIP ensemble. The results highlight the interhemispheric transitional nature of the long rains, with the locations of March and May drivers in opposite hemispheres. Further studies should quantify to what extent the mechanisms for rainfall decline revealed in this study are driven by natural variability, amplified land–ocean pressure gradients driven by anthropogenic carbon emissions and changing aerosol forcings; and the role of these mechanisms under future climate change.

METHODS

Precipitation data

The CHIRPS daily rainfall dataset³⁴ and Tropical Applications of Meteorology using Satellite data and ground-based observations (TAMSAT)³⁵ daily rainfall dataset were used for 1985–2018. Both rainfall datasets use thermal infra-red imagery to calculate rainfall totals; CHIRPS also includes gauge data, a monthly precipitation climatology, and atmospheric model rainfall fields from the NOAA Climate Forecast System, version 2 (CFSv2)³⁴. TAMSAT, however, just uses thermal infra-red imagery; gauge observations are used for the time-invariant calibration but are not incorporated into the estimates³⁵. The Global Precipitation Climatology Project (GPCP) monthly

precipitation analysis was also used over 1985–2018; it uses low-orbit satellite microwave data, geosynchronous-orbit satellite infra-red data, and surface rain gauge observations to calculate rainfall totals³⁶.

Reanalysis data

Geopotential height and wind data were taken from the ERA-Interim reanalysis for 1986–2018, produced by the European Centre for Medium-Range Weather Forecasts (ECMWF), using the Integrated Forecast System combined with data assimilation³⁷.

SST data and correlations

Monthly HadISST (v1.1) observed SST data, produced by the UK Met Office were used for 1986–2018³⁸. In order to compute the uncertainty on the SST correlations, ten different realisations of HadISST (v2.2) were used to compute a range on the correlation values³⁹. These data are only available until 2015, and hence are used for 1986–2015. Correlations were computed using the Pearson Correlation Coefficient, and data were detrended first.

Atmosphere-only model simulations

Atmosphere-only simulations were obtained from 28 models from the CMIP5 generation of models⁴⁰. The atmosphere-only simulations are driven by historical SSTs, sea ice and radiative forcing agents. Daily and monthly precipitation and monthly geopotential height and winds at 850 and 925 hPa were obtained for 1986–2008. Only the first ensemble members (r1i1p1) are used. To enable the construction of multi-model means, the data were re-gridded to a $1^\circ \times 1^\circ$ grid. The models used are listed in Table 1.

Coupled model simulations

Data from 29 coupled climate model simulations, used in CMIP5⁴⁰, were used to assess changes in variables under future climate change. The coupled simulations include a fully coupled ocean and are driven by historical radiative forcings for the observation period and use radiative forcings from representative concentration pathway (RCP) 8.5 for the future projections⁴¹; this is a high emission scenario, with a radiative forcing of 8.5 W m^{-2} at 2100. Only the first ensemble members (r1i1p1) are used. Monthly geopotential height (850 hPa), near-surface air temperature and eastward and northward winds (850 hPa) were obtained for 1980–1999 and 2080–2099. To enable the construction of multi-model means, the data were re-gridded to a $1^\circ \times 1^\circ$ grid for geopotential and temperature, and $3^\circ \times 3^\circ$ for winds. The models used are listed in Table 2.

Onset/cessation methodology

Onset and cessation dates were computed using the methodology of anomalous accumulation, used in a number of studies of seasonality over Africa^{42,43}. This methodology identifies wet seasons when the rainfall is persistent in occurrence, duration and intensity⁴⁴. Full details of the methodology can be found in Dunning et al.⁴³; the two season variant is used here. Firstly, the two periods of the year when the wet seasons occur, labelled the climatological wet seasons, are determined by identifying local minima and maxima in the climatological cumulative daily mean rainfall anomaly. To calculate the climatological cumulative daily mean rainfall anomaly, the climatological mean rainfall for each day of the calendar year, R_i , and the long-term climatological daily mean rainfall, \bar{R} , are computed. The climatological cumulative daily mean rainfall anomaly on day d , is

$$C(d) = \sum_{i=1}^d R_i - \bar{R}, \quad (1)$$

where i ranges from 1st January to the day for which the calculation applies. Local minima and maxima in $C(d)$ determine the beginning and end of the climatological seasons; if the method cannot identify two seasons then the point is excluded from this analysis, as the main interest is the biannual regime over East Africa.

Onset and cessation dates are calculated for each season individually, by calculating the daily cumulative rainfall anomaly for each climatological wet season (starting 20 days prior to the start of the climatological wet season and ending 20 days after the end of the climatological wet season). The minima in the daily cumulative rainfall anomaly is the onset date, and

Table 1. List of AMIP models (and institutions) used in this study. The number in the first column is the symbol used for that model in Fig. 3c

Model number (Fig. 3)	Institute	Model	References
1	CSIRO-BOM	ACCESS 1.0	45
2	CSIRO-BOM	ACCESS 1.3	45
3	BCC	bcc-csm1-1	46
4	BCC	bcc-csm1-1-m	46
5	BNU	BNU-ESM	47
6	CCCma	CanAM4	48
7	NCAR	CCSM4	49
8	CMCC	CMCC-CM	50
9	CNRM-CERFACS	CNRM-CM5	51
10	CSIRO-QCCCE	CSIRO-Mk3-6-0	52
11	ICHEC	EC-EARTH	53
12	LASG-CESS	FGOALS-g2	54
13	NOAA-GFDL	GFDL-CM3	55
14	NOAA-GFDL	GFDL-HIRAM-C180	55
15	NOAA-GFDL	GFDL-HIRAM-C360	55
16	NASA-GISS	GISS-E2-R	56
17	MOHC	HadGEM2-A	57
18	INM	inmcm4	58
19	IPSL	IPSL-CM5A-LR	59
20	IPSL	IPSL-CM5A-MR	59
21	IPSL	IPSL-CM5B-LR	59
22	MIROC	MIROC5	60
23	MPI-M	MPI-ESM-LR	61
24	MPI-M	MPI-ESM-MR	61
25	MRI	MRI-AGCM3-2H	62
26	MRI	MRI-AGCM3-2S	62
27	MRI	MRI-CGCM3	63
28	NCC	NorESM1-M	64

Table 2. List of CMIP5 models and institutions that provided coupled model output used in this study

Institute	Model	References
CSIRO-BOM	ACCESS 1.0	45
CSIRO-BOM	ACCESS 1.3	45
BCC	bcc-csm1-1-m	46
BNU	BNU-ESM	47
CCCma	CanESM2	48
NCAR	CCSM4	49
NSF-DOE-NCAR	CESM1-BGC	65
NSF-DOE-NCAR	CESM1-CAM5	66
CMCC	CMCC-CMS	50
CMCC	CMCC-CM	50
CNRM-CERFACS	CNRM-CM5	51
CSIRO-QCCCE	CSIRO-Mk3-6-0	52
ICHEC	EC-EARTH	53
LASG-CESS	FGOALS-g2	54
NOAA-GFDL	GFDL-ESM2G	67
NOAA-GFDL	GFDL-ESM2M	67
MOHC	HadGEM2-CC	68
MOHC	HadGEM2-ES	68
INM	inmcm4	58
IPSL	IPSL-CM5A-LR	59
IPSL	IPSL-CM5A-MR	59
IPSL	IPSL-CM5B-LR	59
MIROC	MIROC5	60
MIROC	MIROC-ESM-CHEM	69
MIROC	MIROC-ESM	69
MPI-M	MPI-ESM-LR	61
MPI-M	MPI-ESM-MR	61
MRI	MRI-CGCM3	63
NCC	NorESM1-M	64

the maxima is the cessation. Seasons of less than 14 days in length are excluded.

Regions used in the analysis

Harmonic analysis was used to determine the region of East Africa that experiences a biannual regime. Using the CHIRPS daily rainfall data, the amplitude of the first harmonic and second harmonic were computed at each grid point. The ratio was then calculated; if the ratio was greater than 1, i.e., the amplitude of the second harmonic was greater than the amplitude of the first harmonic, then the grid point was defined as biannual. The biannual region was then smoothed using a Gaussian filter to give the region mask shown in Fig. 1c–f. For other datasets (e.g., AMIP data) the same mask was re-gridded.

For the correlations in Fig. 3, the Arabian Heat Low was defined to be 50–75°E, 10–25°N; this region captures the decline in geopotential in both ERA-Interim and the AMIP multi-model mean.

DATA AVAILABILITY

The TAMSAT data set are available from the TAMSAT website (<https://www.tamsat.org.uk/>). The CHIRPS data set, produced by the Climate Hazards Group, is available at <https://chc.ucsb.edu/data/chirps/>. GPCP data provided by the NOAA/OAR/ESRL PSD, Boulder, Colorado, USA, from their website at <https://www.esrl.noaa.gov/psd/>. ERA-I data were sourced from CEDA (<ftp.ceda.ac.uk>).

We acknowledge the World Climate Research Programme's Working Group on Coupled Modelling, which is responsible for CMIP, and we thank the climate modelling groups for producing and making available their model outputs; for CMIP, the US Department of Energy's PCMDI provided coordinating support and led development of software infrastructure in partnership with the Global Organisation for Earth System Science Portals. Model data were sourced from the CMIP5 data portal (http://cmip-pcmdi.llnl.gov/cmip5/data_portal.html) and the British Atmospheric Data Centre (<http://badc.nerc.ac.uk/>) via CEDA (<ftp.ceda.ac.uk>). Monthly HadISST (v1.1) observed SST data are available from <https://www.metoffice.gov.uk/hadobs/hadisst/data/download.html>. The first member of the 10 different realisations of HadISST (v2.2) can be found here: <https://doi.org/10.22033/ESGF/input4MIPs.1221>; the rest are currently restricted until openly published.

CODE AVAILABILITY

Code for computing onset and cessation dates can be obtained from Caroline Wainwright upon request (c.wainwright@reading.ac.uk).

ACKNOWLEDGEMENTS

The authors would like to thank two anonymous reviewers for their insightful and constructive comments. Caroline Wainwright, Declan Finney, John Marsham, David Rowell and Emily Black were supported by the Natural Environment Research Council/Department for International Development (NERC/DFID, NE/ M020371/1, NE/ M02038X/1, and NE/M019985/1) via the Future Climate for Africa (FCFA) funded project, Integrating Hydro-Climate Science into Policy Decisions for Climate-Resilient Infrastructure and Livelihoods in East Africa (HyCRISTAL). John Marsham and Emily Black were also supported by the National Centre for Atmospheric Science via the NERC/GCRF programme Atmospheric hazard in developing countries: risk assessment

and early warning (ACREW). Emily Black also gratefully acknowledges support from the NERC/DFID BRAVE project (NE/M008983/1) and the Global Challenges Research Fund project, SatWIN-ALERT (NE/R014116/1). The contribution of Richard J. Keane was supported through the Centre for Environmental Modelling and Computation (CEMAC), University of Leeds. Richard Allan was funded by the UK National Environment Research Council (NERC) SMURPHS project NE/N006054/1 and the National Centre for Earth Observation LTS-5 grant NE/R016518/.

AUTHOR CONTRIBUTIONS

J.H.M. conceived the study, based on Dunning et al.¹³. C.M.W. analysed the observed rainfall datasets (CHIRPS and TAMSAT), including calculation of onset dates, and the AMIP and CMIP data. CMW completed the SST correlation analysis. R.J.K. analysed GPCP rainfall and ERA-Interim reanalysis (Figs 2a, c, e and 3a, b). CMW constructed Figs 1, 3 and 4; R.J.K. constructed Fig. 2. C.M.W. and J.H.M. led the writing of the paper. All authors interpreted and discussed the results and commented on the figures and the paper.

ADDITIONAL INFORMATION

Supplementary information accompanies the paper on the *npj Climate and Atmospheric Science* website (<https://doi.org/10.1038/s41612-019-0091-7>).

Competing interests: The authors declare no competing interests.

Publisher's note Springer Nature remains neutral with regard to jurisdictional claims in published maps and institutional affiliations.

REFERENCES

- Liebmann, B. et al. Climatology and interannual variability of boreal spring wet season precipitation in the eastern horn of Africa and implications for its recent decline. *J. Clim.* <https://doi.org/10.1175/JCLI-D-16-0452.1> (2017)
- Liebmann, B. et al. Understanding recent eastern horn of Africa rainfall variability and change. *J. Clim.* **27**, 8630–8645 (2014).
- Hoell, A. et al. Reconciling theories for human and natural attribution of recent East Africa drying. *J. Clim.* **30**, 1939–1957 (2017).
- Lyon, B. & DeWitt, D. G. A recent and abrupt decline in the East African long rains. *Geophys. Res. Lett.* **39**, L02702 (2012).
- Lyon, B. Seasonal drought in the Greater Horn of Africa and its recent increase during the March–May long rains. *J. Clim.* **27**, 7953–7975 (2014).
- Rowell, D. P. et al. Reconciling past and future rainfall trends over East Africa. *J. Clim.* **28**, 9768–9788 (2015).
- Williams, A. P. & Funk, C. A westward extension of the warm pool leads to a westward extension of the Walker circulation, drying eastern Africa. *Clim. Dyn.* **37**, 2417–2435 (2011).
- Maidment, R. I., Allan, R. P. & Black, E. Recent observed and simulated changes in precipitation over Africa. *Geophys. Res. Lett.* **42**, 8155–8164 (2015).
- Hua, W. et al. Understanding the Central Equatorial African long-term drought using AMIP-type simulations. *Clim. Dyn.* **50**, 1115–1128 (2018).
- Seager, R. et al. Strengthening tropical Pacific zonal sea surface temperature gradient consistent with rising greenhouse gases. *Nat. Clim. Chang.* **9**, 517–522 (2019).
- Liu, W., Xie, S.-P. & Lu, J. Tracking ocean heat uptake during the surface warming hiatus. *Nat. Commun.* **7**, 10926 (2016).
- Hastenrath, S., Polzin, D. & Mutai, C. Circulation mechanisms of Kenya rainfall anomalies. *J. Clim.* **24**, 404–412 (2011).
- Dunning, C. M., Black, E. & Allan, R. P. Later wet seasons with more intense rainfall over Africa under future climate change. *J. Clim.* **31**, 9719–9738 (2018).
- Dong, B. & Sutton, R. Dominant role of greenhouse-gas forcing in the recovery of Sahel rainfall. *Nat. Clim. Chang.* **5**, 757–760 (2015).
- Evan, A. T., Flamant, C., Lavaysse, C., Kocha, C. & Saci, A. Water vapor-forced greenhouse warming over the Sahara Desert and the recent recovery from the Sahelian drought. *J. Clim.* **28**, 108–123 (2015).
- Smith, E. A. The structure of the Arabian Heat Low. Part I: surface energy budget. *Mon. Weather Rev.* **114**, 1067–1083 (2002).
- Steinhoff, D. F. et al. Influences of the Monsoon Trough and Arabian Heat Low on Summer Rainfall over the United Arab Emirates. *Mon. Weather Rev.* **146**, 1383–1403 (2018).
- Krishnamurti, T. N., Stefanova, L. & Misra, V. *Heat Induced Circulation*. 47–74. https://doi.org/10.1007/978-1-4614-7409-8_4 (2013).
- Smith, E. A. The structure of the Arabian Heat Low. Part II: bulk tropospheric heat budget and implications. *Mon. Weather Rev.* **114**, 1084–1102 (2002).
- Varikoden, H., Revadekar, J. V., Kuttippurath, J. & Babu, C. A. Contrasting trends in southwest monsoon rainfall over the Western Ghats region of India. *Clim. Dyn.* **1–10** (2018).
- Almazroui, M., Islam, M. N., Jones, P. D., Athar, H. & Rahman, M. A. Recent climate change in the Arabian Peninsula: seasonal rainfall and temperature climatology of Saudi Arabia for 1979–2009. *Atmos. Res.* **111**, 29–45 (2012).
- Attada, R. et al. Surface air temperature variability over the Arabian Peninsula and its links to circulation patterns. *Int. J. Climatol.* **39**, 445–464 (2019).
- Nicholson, S. E. Climate and climatic variability of rainfall over Eastern Africa. *Rev. Geophys.* **55**, 590–635 (2017).
- Vellinga, M. & Milton, S. F. Drivers of interannual variability of the East African “Long Rains”. *Q. J. R. Meteorol. Soc.* **144**, 861–876 (2018).
- Hsu, N. C. et al. Global and regional trends of aerosol optical depth over land and ocean using SeaWiFS measurements from 1997 to 2010. *Atmos. Chem. Phys.* **12**, 8037–8053 (2012).
- Solmon, F., Nair, V. S. & Mallet, M. Increasing Arabian dust activity and the Indian summer monsoon. *Atmos. Chem. Phys.* **15**, 8051–8064 (2015).
- Okoola, R. E. Spatial evolutions of the active convective patterns across the equatorial Eastern Africa region during Northern hemisphere spring season using outgoing longwave radiation records. *Meteorol. Atmos. Phys.* **66**, 51–63 (1998).
- Hastenrath, S., Nicklis, A. & Greischar, L. Atmospheric-hydrospheric mechanisms of climate anomalies in the Western Equatorial Indian Ocean. *J. Geophys. Res.* **98**, 20219–20235 (1993).
- Sutton, R. T., Dong, B. & Gregory, J. M. Land/sea warming ratio in response to climate change: IPCC AR4 model results and comparison with observations. *Geophys. Res. Lett.* **34**, L02701 (2007).
- Marsham, J. H. et al. The contrasting roles of water and dust in controlling daily variations in radiative heating of the summertime Saharan heat low. *Atmos. Chem. Phys.* **16**, 3563–3575 (2016).
- Munday, C. & Washington, R. Systematic climate model rainfall biases over Southern Africa: links to moisture circulation and topography. *J. Clim.* **31**, 7533–7548 (2018).
- Shongwe, M. E., van Oldenborgh, G. J., van den Hurk, B. & van Aalst, M. Projected changes in mean and extreme precipitation in Africa under global warming. Part II: East Africa. *J. Clim.* **24**, 3718–3733 (2011).
- Vizy, E. K. & Cook, K. H. Mid-twenty-first-century changes in extreme events over Northern and Tropical Africa. *J. Clim.* **25**, 5748–5767 (2012).
- Funk, C. et al. The climate hazards infrared precipitation with stations—a new environmental record for monitoring extremes. *Sci. Data* **2**, 150066 (2015).
- Maidment, R. I. et al. A new, long-term daily satellite-based rainfall dataset for operational monitoring in Africa. *Sci. Data* **4**, 170063 (2017).
- Adler, R. F. et al. The version-2 Global Precipitation Climatology Project (GPCP) monthly precipitation analysis (1979–present). *J. Hydrometeorol.* **2**, (2003). [https://doi.org/10.1175/1525-7541\(2003\)0042.0.CO;2](https://doi.org/10.1175/1525-7541(2003)0042.0.CO;2)
- Dee, D. P. et al. The ERA-Interim reanalysis: configuration and performance of the data assimilation system. *Q. J. R. Meteorol. Soc.* **137**, 553–597 (2011).
- Rayner, N. A. et al. Global analyses of sea surface temperature, sea ice, and night marine air temperature since the late nineteenth century. *J. Geophys. Res.* **108**, 4407 (2003).
- Kennedy, J., Titchner, H., Rayner, N. & Roberts, M. input4MIPs.MOHC.SSTsAnd-SeaIce.HighResMIP.MOHC-HadISST-2-2-0-0-0. Version 20170505. *Earth Syst. Grid Fed.* (2017) <https://doi.org/10.22033/ESGF/input4MIPs.1221>.
- Taylor, K. E., Stouffer, R. J. & Meehl, G. A. An overview of CMIP5 and the experiment design. *Bull. Am. Meteorol. Soc.* **93**, 485–498 (2012).
- Van Vuuren, D. P. et al. The representative concentration pathways: an overview. *Clim. Change* **109**, 5 (2011).
- Liebmann, B. et al. Seasonality of African precipitation from 1996 to 2009. *J. Clim.* **25**, 4304–4322 (2012).
- Dunning, C. M., Black, E. C. L. & Allan, R. P. The onset and cessation of seasonal rainfall over Africa. *J. Geophys. Res. Atmos.* **121**, 11405–11424 (2016).
- Diaconescu, E. P., Gachon, P., Scinocca, J. & Laprise, R. Evaluation of daily precipitation statistics and monsoon onset/retreat over western Sahel in multiple data sets. *Clim. Dyn.* **45**, 1325–1354 (2015).
- Bi, D. et al. The ACCESS coupled model: description, control climate and evaluation. *Aust. Meteorol. Ocean.* **63**, 41–64 (2013).
- Wu, T. et al. An overview of BCC climate system model development and application for climate change studies. *J. Meteorol. Res.-PRC* **28**, 34–56 (2014).
- Ji, D. et al. Description and basic evaluation of Beijing Normal University Earth system model (BNU-ESM) version 1. *Geosci. Model Dev.* **7**, 2039–2064 (2014).
- Arora, V. K. et al. Carbon emission limits required to satisfy future representative concentration pathways of greenhouse gases. *Geophys. Res. Lett.* **38**, L05805 (2011).
- Gent, P. R. et al. The community climate system model version 4. *J. Clim.* **24**, 4973–4991 (2011).

50. Fogli, P. G. et al. INGV-CMCC carbon (ICC): a carbon cycle earth system model. *C. Research Paper No. 61* (2009).
51. Voldoire, A. et al. The CNRM-CM5. 1 global climate model: description and basic evaluation. *Clim. Dyn.* **40**, 2091–2121 (2013).
52. Jeffrey, S. J. et al. Australia's CMIP5 submission using the CSIRO Mk3. 6 model. *Aust. Meteor. Ocean. J.* **63**, 1–13 (2013).
53. Hazeleger, W. et al. EC-Earth V2. 2: description and validation of a new seamless earth system prediction model. *Clim. Dyn.* **39**, 2611–2629 (2012).
54. Li, L. et al. The flexible global ocean-atmosphere-land system model, Grid-point Version 2: FGOALS-g2. *Adv. Atmos. Sci.* **30**, 543–560 (2013).
55. Delworth, T. L. et al. GFDL's CM2 global coupled climate models. Part I: formulation and simulation characteristics. *J. Clim.* **19**, 643–674 (2006).
56. Schmidt, G. A. et al. Present-day atmospheric simulations using GISS ModelE: comparison to in situ, satellite, and reanalysis data. *J. Clim.* **19**, 153–192 (2006).
57. Collins, M., Tett, S. F. B. & Cooper, C. The internal climate variability of HadCM3, a version of the Hadley Centre coupled model without flux adjustments. *Clim. Dyn.* **17**, 61–81 (2001).
58. Volodin, E. M., Dianskii, N. A. & Gusev, A. V. Simulating present-day climate with the INMCM4. 0 coupled model of the atmospheric and oceanic general circulations. *Izv. Atmos. Ocean. Phys.* **46**, 414–431 (2010).
59. Dufresne, J.-L. et al. Climate change projections using the IPSL-CM5 Earth System Model: from CMIP3 to CMIP5. *Clim. Dyn.* **40**, 2123–2165 (2013).
60. Watanabe, M. et al. Improved climate simulation by MIROC5: mean states, variability, and climate sensitivity. *J. Clim.* **23**, 6312–6335 (2010).
61. Stevens, B. et al. Atmospheric component of the MPI-M Earth System Model: ECHAM6. *J. Adv. Model. Earth Syst.* **5**, 146–172 (2013).
62. Mizuta, R. et al. Climate simulations using MRI-AGCM3. 2 with 20-km grid. *J. Meteorol. Soc. Jpn. Ser. II* **90**, 233–258 (2012).
63. Yukimoto, S. et al. Meteorological Research Institute Earth System Model Version 1 (MRI-ESM1): Model Description-Technical reports of the meteorological research institute No. 64. *Meteorological Research Institute, Japan* (2011).
64. Iversen, T. et al. The Norwegian earth system model, NorESM1-M-Part 2: climate response and scenario projections. *Geosci. Model Dev. Discuss.* **5**, 2933–2998 (2012).
65. Long, M. C., Lindsay, K., Peacock, S., Moore, J. K. & Doney, S. C. Twentieth-century oceanic carbon uptake and storage in CESM1 (BGC). *J. Clim.* **26**, 6775–6800 (2013).
66. Hurrell, J. W. et al. The community earth system model: a framework for collaborative research. *Bull. Am. Meteorol. Soc.* **94**, 1339–1360 (2013).
67. Dunne, J. P. et al. GFDL's ESM2 global coupled climate-carbon earth system models. Part I: physical formulation and baseline simulation characteristics. *J. Clim.* **25**, 6646–6665 (2012).
68. Collins, W. J. et al. Development and evaluation of an Earth-System model-HadGEM2. *Geosci. Model Dev.* **4**, 1051–1075 (2011).
69. Watanabe, S. et al. MIROC-ESM 2010: Model description and basic results of CMIP5-20c3m experiments. *Geosci. Model Dev.* **4**, 845 (2011).



Open Access This article is licensed under a Creative Commons Attribution 4.0 International License, which permits use, sharing, adaptation, distribution and reproduction in any medium or format, as long as you give appropriate credit to the original author(s) and the source, provide a link to the Creative Commons license, and indicate if changes were made. The images or other third party material in this article are included in the article's Creative Commons license, unless indicated otherwise in a credit line to the material. If material is not included in the article's Creative Commons license and your intended use is not permitted by statutory regulation or exceeds the permitted use, you will need to obtain permission directly from the copyright holder. To view a copy of this license, visit <http://creativecommons.org/licenses/by/4.0/>.

© The Author(s) 2019